96-Channel Receive-Only Head Coil for 3 Tesla: Design Optimization and Evaluation

Graham C. Wiggins[1,*], **Jonathan R. Polimeni**[1], **Andreas Potthast**[2], **Melanie Schmitt**[1], **Vijay Alagappan**[1], and **Lawrence L. Wald**[1,3]

[1] Department of Radiology, Massachusetts General Hospital, Charlestown, Massachusetts, USA

[2] Siemens Healthcare, Erlangen, Germany

[3] Harvard-MIT Division of Health Sciences Technology, Cambridge, Massachusetts, USA

Abstract

The benefits and challenges of highly parallel array coils for head imaging were investigated through the development of a 3T receive-only phased-array head coil with 96 receive elements constructed on a close-fitting helmet-shaped former. We evaluated several designs for the coil elements and matching circuitry, with particular attention to sources of signal-to-noise ratio (SNR) loss, including various sources of coil loading and coupling between the array elements. The SNR and noise amplification (*g*-factor) in accelerated imaging were quantitatively evaluated in phantom and human imaging and compared to a 32-channel array built on an identical helmet-shaped former and to a larger commercial 12-channel head coil. The 96-channel coil provided substantial SNR gains in the distal cortex compared to the 12- and 32-channel coils. The central SNR for the 96-channel coil was similar to the 32-channel coil for optimum SNR combination and 20% lower for root-sum-of-squares combination. There was a significant reduction in the maximum *g*-factor for 96 channels compared to 32; for example, the 96-channel maximum *g*-factor was 65% of the 32-channel value for acceleration rate 4. The performance of the array is demonstrated in highly accelerated brain images.

Keywords

phased array; 96-channel; RF coil design; SNR; *g*-factor

The benefits of radio frequency (RF) receive-coil arrays of up to 32 channels have been demonstrated for the brain (1–7) and heart (8–12). Based on these successes, a limited number of studies have explored the potential advantages of even higher element numbers for a small bore scanner (13,14) as well as for brain (15,16) and cardiac imaging (17,18). As the number of receive-array channels increases, theoretical analysis predicts that it is possible to reduce the size of the individual elements and achieve increasing signal-to-noise ratio (SNR) gains near the elements without losing sensitivity further from the coils (1), in addition to improved encoding acceleration performance (19,20). These theoretical studies have usually assumed perfect decoupling between the array coil elements and body noise dominant conditions. Wiesinger (19) and Wiesinger et al. (20) performed simulations of a spherical object surrounded by various numbers of coil elements, using semianalytical expressions for the full-wave RF electrodynamic field, incorporating copper losses in the coils, preamplification (preamp) noise contributions and the noise covariance between the

---

*Correspondence to: Graham Wiggins, D.Phil, A. A. Martinos Center for Biomedical Imaging, Bldg. 149 13th Street, Mailcode 149-2301, Charlestown, MA 02129. gwiggins@nmr.mgh.harvard.edu.

coil elements. The simulations did not take into account radiation losses or inductive coupling between the coil elements. For a 20-cm sphere with dielectric properties corresponding to average brain values, these simulations suggest that at 3T the ultimate possible SNR is already closely approached at the center of the sample when it is surrounded by 32 or more coil elements. For regions closer to the surface, increasing numbers of smaller elements are required to approach the ultimate SNR and the benefit of adding elements is roughly linear in the number of elements. In contrast, if coil noise is dominant over body noise (a concern for small elements and/or low B_0 field), SNR eventually decreases with increasing numbers of elements.

These considerations have led us to pursue designs in which many small array elements are placed on a close-fitting helmet to maximize the body load. Nevertheless, in a previous work where we constructed a 90-channel head array for 1.5T (15), we appear to have encountered the limitation posed by coil noise dominance, as this array showed significantly lower central SNR compared to a 23-channel array constructed on an identical helmet former. Guided by this work and the theoretical simulations, we analyzed several design changes aimed at decreasing the losses in the unloaded array and reducing inductive coupling between the surface coil elements. In this work, we describe a 96-channel head array for 3T with the same element geometry as the 90-channel 1.5T coil but with a significantly improved unloaded to loaded Q ratio (body noise dominance). The array was evaluated in phantom and human measurements for SNR, g-factor, and noise covariance, and compared to a 32-channel head array built on an identical former, and also to a commercially-available 12-channel coil.

MATERIALS AND METHODS

The arrays were developed and tested on a 32-channel 3T clinical scanner (MAGNETOM Trio, A Tim System; Siemens Healthcare, Erlangen, Germany). The 3T scanner had 96 additional receive channels, making 128 channels available in total (21). Only 96 of the available 128 channels were used for the 3T helmet array. All human subject studies were performed after review by the institution's Human Research Committee and informed consent was obtained from the subject.

Array Construction

The geometrical arrangement of the circular coil elements was an extension of the "soccer-ball" geometry described previously for a 32-channel helmet array (2). A tiling pattern consisting of hexagons and pentagons is created. The centers of the tiles determine the centers of the circular coil elements, with larger-diameter coils at the positions corresponding to the hexagonal tiles, and smaller ones over the pentagonal tiles. For the 96-channel coil, the geometry of the C240 carbon "Buckyball" was used as the basis for the placement of the coil elements, using one half of the spherical molecule structure to cover the dome of the head and extending the lattice downward on a cylinder (Fig. 1, left). Although the majority of coils are arranged in a hexagonal, honeycomb pattern, there are six centers of pentagonal symmetry in the lattice, which are essential to allow the array to wrap over the entire dome of the head in a continuous overlapped design that minimizes inductive coupling between neighboring coil elements. The coils were arranged on a close-fitting fiberglass helmet modeled after the European standard head norm EN960/1994 for protective headgear (22) (Fig. 1, right). The dimensions of all coils discussed in this work are given in Table 1. To determine the layout of the coil elements on the helmet, a paper mock-up was made, consisting of hexagonal and pentagonal tiles covering the helmet. Each paper tile had sides of 23 mm, and the entire shape incorporated 90 hexagons and six pentagons. The vertex of each tile was marked on the helmet and used to reproduce the tiling pattern on the surface of the helmet (Fig. 1, right). This pattern was used to determine the

position of the circular surface coils, with each element approximately circumscribing a hexagonal or pentagonal tile. Most areas of the helmet had coils that had a pitch, or offset between one element and the next one in the row, of 39.8 mm. The final position of the coil element conductors was determined empirically based on minimizing inductive coupling to neighbors.

A number of different element designs were constructed and assessed, including elements machined from FR4 circuit board material and elements fashioned from wire of various thicknesses. The dimensions of the various element designs had to satisfy one key criterion: when placed at the positions defined by the tiling pattern on the helmet, they had to overlap their neighbors by the critical amount that nulls inductive coupling. Elements constructed of half-ounce copper-clad FR4 circuit board with different track widths or made from wire each required a different inside diameter and percentage overlap to satisfy this condition. The element designs are summarized in Table 2.

The unloaded to loaded Q ratio (Q_{UL}/Q_L) for each element design was determined for an individual element with no cable attached using an S_{12} measurement between two shielded inductive probes loosely coupled to the coil element. Loaded Q was measured with each coil element 13 mm from an 8-liter rectangular doped water phantom with 3.3685 g/liter $NiCl_2 \cdot 6H_2O$ + 2.4 g/liter NaCl (USA Instruments, Aurora, OH, USA). For four of the element designs Q_{UL}/Q_L was also assessed when the individual element was surrounded by the conductors of six nonresonant overlapped neighboring elements to determine the effect of copper loading from the conductors of other coil elements. Active detuning was measured for an unloaded coil element as the change in S_{12} between decoupled inductive probes when bias was applied to the positive-intrinsic-negative (PIN) diode. Preamp decoupling strength was measured for an unloaded coil element as the change in S_{12} between the decoupled inductive probes when the coil was matched to a 50-Ohm load or when preamp decoupling was active and the preamp was powered. Isolation between pairs of coil elements was determined from an S_{12} measurement with each coil matched to 50 Ohms and attached with coax to a port of the network analyzer and all other coil elements detuned.

The final coil design incorporated wire coil elements (18-awg tinned copper wire) with an inner diameter of 50 mm for the hexagonal tile positions and 42 mm for the pentagonal tile positions. Each loop incorporated two capacitors (Fig. 2). A tool was constructed to form the wire segments into the desired shape, with appropriate "humps" to bridge over wires from adjacent coils. A framework of copper pads was created by machining FR4 circuit board material into a shape that traced the expected tracks of the wire conductors but had all of the copper machined off except where the pads were needed. All other material was cut away, leaving a flexible matrix that could be wrapped around the helmet and secured with Nylon screws, maintaining registration to the tiling pattern previously applied to the helmet. The wire segments, tune and match capacitors, and trimmer capacitors were soldered to this framework. A detuning circuit was formed across the match capacitor using a hand-wound inductor and a PIN diode (Macom MA4P4002B-402; Macom, Lowell, MA, USA). A six-pin socket was soldered to each coil element with three pins connected in common to each side of the match capacitor. All components of the detuning circuit were constructed around the match capacitor and directly connected to the wire conductors of the coil element, to avoid the losses from routing the circuit through the socket connector that were revealed in an earlier intermediary design. Individual elements could be passively detuned during construction by pushing a wire "jumper" into the socket to effectively complete the detuning circuit. S_{12} coupling between neighboring, overlapped coils was minimized by bending the wire conductors. Figure 3 shows a close-up of the array elements for both an abandoned design using circuit board elements and the final wire-based design.

Preamp assemblies mounted on small circuit boards (18 mm × 88 mm) were connected to the array elements though the six-pin socket. The preamp assembly board included 70 mm of semirigid coax to provide the desired phase length to provide preamp decoupling but coiled back on itself to reduce the overall length. The preamplifiers used (Siemens Healthcare, Erlangen Germany) incorporate a two-stage amplification with a common mode rejection filter between the two stages (23). The preamp outputs were connected to the scanner with 1.18 mm mini-coax cable. The first 32 channels were connected via the standard coil plugs at the head end of the patient table, while the additional channels were connected via coax bundles run through the bore of the magnet to the additional receive electronics at the rear of the scanner room. Bias for the active detuning of the array elements was supplied from 32 PIN bias lines from the patient table plugs. Each bias line was split three ways to bias three coil elements in parallel. Resistors of 147 Ohms were placed in series with each bias line near the coil element to ensure nearly equal splitting of the 100-mA bias current between the three shared elements. The preamps also contain a bias-T for the PIN diode bias. A single bias line was connected to the bias-T on each preamp, with the RF coax ground serving as the bias current return path. The bias wires were wrapped around the RF coax to avoid creating any open loop through which significant flux could penetrate and induce current in the wire. The completed coil is shown in Fig. 4.

Performance Measurements

For SNR comparison, proton density–weighted gradient-echo images (TR/TE/flip angle = 200 ms/3.92 ms/20°, slice = 3 mm, matrix size = 256 × 256, field of view [FOV] = 220 mm, bandwidth [BW] = 300 Hz/pixel) were obtained in the sagittal, axial, and coronal planes in human subjects. To isolate the effect of increasing the number of elements in an array, results were compared using a 32-channel phased array constructed on an identical helmet former (2). For comparison to widely available head coils, SNR data were also acquired with a 12-channel matrix head coil (Siemens Healthcare) with considerably larger overall dimensions (Table 1). The 12-channel matrix array was used in "Triple Mode" (all 12 channels recorded and used in the reconstruction) (24).

For each acquisition, raw k-space data were saved for analysis, and magnitude images reconstructed online were also saved for comparison. A noise reference measurement was obtained by recording complex-valued data during the same pulse sequence used for the image acquisition with no RF excitation. The noise covariance was calculated from the noise samples and then scaled by the noise equivalent BW to account for noise correlations caused by the filtering introduced by the data acquisition electronics and receiver (25). Individual coil images were then reconstructed, and estimates of the coil sensitivity profiles were generated by low-pass filtering the image intensities with a two-dimensional (2D) Hanning filter (normalized for unity noise gain) with a full-width at half-maximum set to include only the central 25% of k-space. This degree of smoothing has been found appropriate for reducing the artificial increase in calculated g-factor caused by image noise, and for removing intensity variations due to anatomy when in vivo data is used.

SNR maps were calculated from the estimates of the coil sensitivity and noise covariance for both the optimal SNR and root-sum-of-squares combination (26), then corrected on a pixel-by-pixel basis for SNR bias introduced by the magnitude detection (25,27). SNR was compared using color scale SNR maps and SNR profiles through the brain.

For g-factor comparison, raw k-space data were acquired in a transverse slice through the center of a 170-mm diameter spherical "Braino" phantom using a FOV tight on the phantom (TR/TE/flip angle = 200 ms/3.6 ms/20°, slice = 3 mm, matrix size = 128 × 128, FOV = 175 mm, BW = 300 Hz/pixel). The phantom dielectric properties were measured with an Aglient 85070E Dielectric Probe (Agilent Technologies, Palo Alto, CA, USA) and it was found to

have a conductivity of 0.97 S/m and relative permittivity of 81.31, both somewhat higher than the average values of 0.46 S/m and 63.1 for the human head at 123 MHz (28). Sensitivity maps and noise covariance matrices were estimated as described above, and sensitivity encoding (SENSE) *g*-factor maps were calculated directly from its analytic expression (29). Because errors in the sensitivity map estimation can be amplified when computing the *g*-factor, the calculation was mildly regularized by diagonal loading (30) with regularization parameter lambda set to 1 for all calculations. Image SNR was calculated for both the full image acquisition and the accelerated acquisition, and their ratio (normalized by the square root of the reduction factor) provided the *g*-factor. Prior to computing the ratio, a constant c = 1 was added to both the numerator and denominator to avoid further errors resulting from small values in the denominator. The *g*-factor maps were plotted as the inverse *g*-factor, 1/*g* (which represents the percentage of SNR retained in a SENSE reconstruction), to allow all of the maps to be shown with the same color scale. The maximum *g*-factor for each acceleration was also recorded. Accelerated imaging is demonstrated with single-shot spin-echo echo planar imaging (EPI) images ($1 \times 1 \times 2$ mm^3, matrix size = 224×224, TR/TE/flip = 4000 ms/63 ms/90°, BW = 1065 Hz/pixel, averages = 16) with generalized autocalibrating partially parallel acquisitions (GRAPPA) acceleration factors from 3 to 7 in the anterior–posterior direction.

RESULTS

Q_{UL}/Q_L Optimization Results

Table 2 shows the *Q* ratio results for the individual coil element designs as measured for isolated single loop coils. Q_{UL}/Q_L for coil elements machined from FR4 circuit board with 2.5-mm track width and six capacitors was only 3.0, indicating that sample noise was just barely dominating coil noise. The same element design was used in the 1.5T 90-channel coil, and thus even the increased load at 3T did not solve the problem of poor coil loading for these small elements. When the track width was increased to 5 mm, Q_{UL}/Q_L increased to 3.7, and was further increased to 5.0 by reducing the number of capacitors from six to two. While this *Q* ratio shows that the single isolated coil can be sample noise-dominated, there are additional loss mechanisms present in the completed array. When the two-capacitor 5-mm trace-width circuit board coil element was surrounded by the conductor segments from its six nearest neighbor coils, Q_{UL}/Q_L dropped to 3.9. Thus losses in the copper from other elements in the array present a significant additional source of noise. In addition to the losses, the resonant frequency of the circular array element was also increased by 1.3 MHz due to the presence of the surrounding copper, indicating that the losses were primarily due to the generation of eddy currents in the copper of the neighboring coils, which also screened the inductance of the element, increasing its frequency.

To reduce the cross-sectional area presented by the conductors to fields created by other coils, wire coil elements were examined. While the coil element consisting of 2.3-mm-diameter copper wire had Q_{UL}/Q_L of 5.1, the highest of all the designs (Table 2), it was too thick to conveniently form the shapes required. It is possible that annealing the copper or using tubing would have made it more accommodating, but we decided to construct the coil elements using 18-awg (1.15 mm measured diameter) tinned copper wire, which had a Q_{UL}/Q_L of 4.1 for a single isolated element. When this wire-based element was placed into a matrix of conductor segments for six surrounding wire-based coils, Q_{UL}/Q_L only dropped to 4.0, with no measurable shift in frequency, demonstrating a significant reduction in copper losses compared to the circuit board coil element designs. Figure 3 demonstrates the reduction in copper coverage with the wire coil design. The percentage area covered with copper in the completed array for the three designs, including pads as well as coil element conductors, was 35% for the 2.5-mm track-width elements, 59% for the 5-mm track-width elements and 14% for the 18-awg wire coil elements. Examining a single active coil element

within the fully-completed helmet array showed Q_{UL}/Q_L of 2.9 when using the human head as a load, separated from the coil element by 13 mm. This lower value can be attributed to loading by the additional coil element conductors, the plugs and circuit boards making up the completed array, and to the fact that the head does not load the coils as much as the phantom at the same coil to sample distance. A phantom was used for the original Q_{UL}/Q_L measurements to obtain the most consistent and repeatable comparisons between element designs.

Preamplifier Decoupling and Active Detuning

In the coil element design shown in Fig. 2, the capacitor C_m serves three functions: 1) it transforms the sample impedance seen by the coil to the impedance required at the preamp for minimum noise value; 2) it forms part of the active detuning circuit (in combination with the PIN diode and inductor); and 3) it provides preamp decoupling when the impedance of the preamp is transformed to a virtual short at the coil. Unfortunately, for these small coil elements, if the sample impedance is transformed to 50 Ohms at the preamp input, a 200-pF capacitor is required. This creates a very low Q detuning circuit and hence provides weak preamp detuning. Matching the coil to 50 Ohms at this point provided a preamplifier decoupling strength of −18 dB, allowing an unacceptable level of inductive coupling between the array elements, reducing sensitivity (31). However, with the preamps used in the final design (23) we were able to achieve the appropriate noise match with C_m equal to 82 pF, increasing the Q of the detuning circuit and strengthening the preamp decoupling to −23 dB.

Because of the design of the 96-channel coil, many of the preamps were positioned so that the main static magnetic field of the scanner was oriented perpendicular to the plane of the preamp board. We discovered that in this orientation the input phase of the preamp was changed when it was in the scanner bore, resulting in a shift of 0.7 MHz in the position of the preamp decoupling minimum. This shift was enough to reduce the preamp decoupling strength by as much as 5 dB, and was corrected by measuring the decoupling minimum with the coil in the scanner and fine tuning the capacitor on the preamp input tank circuit to compensate. No such shift was observed for preamps where the main static magnetic field lies in the plane of the preamp board. This dependence of preamp phase on orientation has also been noticed in a different manufacturer's preamp by another research group (32).

With the 100-mA bias current split between three coils, the active PIN diode detuning (33 mA per element) was −33.5 dB. With the standard 100-mA current through a single element, active detuning only increased to −37.5 dB. The S_{12} coupling between neighboring coils was minimized by distorting the wire conductors, achieving an average S_{12} coupling of −17 dB, with the maximum nearest neighbor coupling equal to −12 dB. The interaction of the coil array with the body coil transmit RF field was examined by noting the scanner transmitter calibration for a large cylindrical phantom placed in the coil array, or placed in the scanner bore with no array present. The body coil RF voltage required for a 1-ms slice-selective hard pulse to create a 180° flip angle changed by =2 V, from 315 V to 317 V, indicating sufficient coil element detuning and suppression of common mode currents on the cables.

SNR and Noise Covariance Performance Comparisons

SNR maps for optimum SNR combination (26) are shown in Fig. 5. SNR profiles taken through an axial slice just above the corpus callosum are shown in Fig. 6, both for optimum SNR and the root-sum-of-squares combination. With the optimum SNR combination, the 96-channel coil provides 5% lower central SNR than the identically-sized 32-channel coil but achieves =1.4-fold higher SNR in the extreme periphery of the brain. Both the 96- and

32-channel coils have about 1.5-fold higher central SNR than the 12-channel product coil with optimum SNR combination. The central SNR increase with respect to the 12-channel coil can likely be attributed to the fact that the dimensions of the 12-channel coil are about 30% larger than the other two coils (Table 1). With the root-sum-of-squares combination—the algorithm that is typically employed for online image reconstruction on the scanner—the 96-channel coil shows 20% lower central SNR than the 32-channel coil, but still shows at least 1.5-fold higher SNR in the outermost parts of the brain. Both the 32- and 96-channel coils show notably high SNR at the apex, demonstrating the utility of placing surface coil elements over the entire dome of the head, despite the fact that many of these elements are oriented with their normal axis close to the *z*-axis. The maximum noise correlation coefficient was 0.43, 0.47, and 0.53, and the average of the off-diagonal elements was 0.127, 0.110, and 0.148 for the 12-, 32-, and 96-channel coils, respectively.

Accelerated Imaging Performance

Figure 7 shows the *g*-factor results for the three arrays for 1D acceleration in the RL direction, and for 2D acceleration (right–left [RL] and AP direction). Figure 8 summarizes the maximum *g*-factor for the 1D acceleration. The benefits of increased channel number for reducing *g*-factor are clear. For example, at acceleration rate 4, the maximum *g*-factor for the 96-channel coil is only 65% of that of the 32-channel coil. For the 2D acceleration, the maximum *g*-factor for 4 × 4 acceleration for the 96-channel array was 43% of the 32-channel coil value. Figure 9 shows single-shot spin-echo EPI acquired with 0.9-mm in-plane resolution and acceleration factors of four- to seven-fold. Relatively artifact-free reconstruction is achieved through an acceleration factor of 6.

DISCUSSION

This study shows that a 96-channel brain array at 3T can achieve significant improvements in peripheral SNR compared to a 32-channel coil built on the same helmet. In the center of the brain, essentially the same SNR is achieved with both coils, and in the periphery of the brain, the 96 channel coil provides a 40% boost in SNR, but only when the optimum SNR combination is used. These results are in qualitative agreement with the reports of Wiesinger (19) and Wiesinger et al. (20) who modeled spherical distributions of circular coils. For the root-sum-of-squares combination the higher noise covariance present in the 96-channel coil causes the central SNR to be 20% lower compared to the 32-channel coil. Near the periphery of the brain, optimum SNR combination offers up to 40% higher SNR than the root-sum-of-squares combination. This is in contrast to the maximum boost of approximately 10% claimed by Roemer et al. (26), but is comparable to gains reported by other authors (33). As the number of receive elements increases, the benefits of taking noise covariance into account by using the optimum SNR combination become increasingly large. If receive arrays with very high numbers of elements become more widely used, the routine implementation of optimum SNR combination online on the scanner will be essential to realize the full potential of such arrays. Improvements to the coil design such as optimization of preamp decoupling, modifications of electric fields through capacitor placement, or gapped designs might also ease the SNR penalty for the root-sum-of-squares combination if noise covariance could be reduced. The *g*-factor improvement in moving from 32 to 96 channels is significant. Thus for accelerated imaging the resulting SNR is higher with the 96-channel coil than the 32-channel coil, particularly for high acceleration rates, due to the much lower noise amplification. The simulations of Refs. [19] and [20] predict a 21% reduction in *g*-factor in moving from 32 to 64 channels for acceleration rate 3.6. Our data show a 31% decrease in maximum *g*-factor in moving from 32 to 96 channels for acceleration rate 4, which is qualitatively in line with the simulations given the higher channel number and acceleration rate in our experimental data.

As the number of coil elements used to cover a given volume increases, the individual element size necessarily decreases. Ultimately, for very high numbers of coils the element size becomes too small and sample noise dominance no longer applies, resulting in a decrease in SNR compared to arrays with fewer elements. At 3T the 50-mm inner diameter coil elements in our 96-channel coil are already on the edge of sample noise dominance, even for a close-fitting helmet and after optimization of the element design. This suggests that similar open-faced head coil designs with higher numbers of coil elements are unlikely to provide SNR benefits for unaccelerated imaging at this field strength without a significant design alteration, such as cooling the conductors or using multiturn coil elements whose higher B_1 efficiency couples them more strongly to the sample. At higher field strengths the increased sample losses may make head coils with even higher numbers of channels advantageous, as long as the considerable engineering challenges of controlling common mode cable currents at higher frequency can be met.

Decreasing the element size also requires attention to the match and active detuning circuitry, as well as the effectiveness of preamp decoupling, since designs that perform well for larger coils can become problematic for small coils. In particular, the use of a simple capacitive match with a PIN diode detuning trap built around the match capacitor becomes problematic for small coil elements for which the match capacitor required becomes larger and larger, reducing the Q of the detuning trap and weakening the preamp decoupling effect. Although optimum SNR combination can recover some of the SNR lost to coupling, some SNR is nevertheless lost due to residual inductive coupling in the presence of preamp decoupling (31), and for coil elements that are not body noise– dominated (34). This problem could also be addressed through alternative, but somewhat more complex, matching and detuning circuit schemes (35).

For small coil elements with marginal $Q_{\mathrm{UL}}/Q_{\mathrm{L}}$, the influence of loss mechanisms external to the body becomes increasingly significant. Reducing the number of capacitors in each element from six to two increased the unloaded Q almost 1.5-fold, demonstrating that distributed capacitance is not always beneficial. We also found that copper losses due to the presence of the conductors making up the other elements in the array had a significant negative impact on the SNR of the array. Reducing the area presented by the conductors by using wire instead of circuit board significantly improved the performance of this array. Using wire instead of copper tape or circuit board will not always be advantageous, but it provided a benefit with this design because of the poor $Q_{\mathrm{UL}}/Q_{\mathrm{L}}$ of the individual elements and the high percentage of copper coverage in the circuit board coil element design. We found the wire design also had several other advantages. Since the bridges over the conductors of neighboring coils were formed by simply bending the wire rather than having to solder in a bridge made of copper tape or wire, we minimized the number of solder joints, each of which contributes to losses and potential failure points in the coil. The wire elements also exhibited significantly reduced capacitive coupling between elements, which could clearly be seen when the coil overlap was adjusted to minimize S_{21}. With circuit board elements the minimum coupling that could be achieved was often only about −11 dB, whereas with wire elements coupling could generally be reduced to −15 dB or better for all neighboring coils. Because of the close proximity of the antenna structure to the sample, minor susceptibility effects could be seen in the vicinity of the trap circuit in phantom images, but are not readily apparent in vivo.

It should also be noted that increasing the number of array channels places an increased computational burden on the image reconstruction computer. This can increase reconstruction times substantially, especially for accelerated imaging. For unaccelerated imaging, root sum of squares reconstruction time increases linearly with the number of channels. Optimum SNR reconstruction does not necessarily incur a significantly greater

penalty in reconstruction time, since only simple matrix inversions and multiplications are required. It is necessary, however, to measure and calculate the noise covariance matrix and the coil sensitivity maps for optimum SNR reconstruction, though these may in principle be performed once per scan session. These problems will be reduced as faster computers become available. Furthermore, the use of 64-bit architectures has proven advantageous for raw data sizes that exceed the address space of 32-bit processors.

CONCLUSIONS

A 3T 96-channel close-fitting helmet phased-array coil has been constructed and tested in human brain imaging. This coil provided significant SNR improvements in the brain cortex and for accelerated imaging compared to an identically-sized 32-channel array. Although the array sensitivity is highest in the cortex, the sensitivity is not significantly lowered anywhere in the brain compared to the 32-channel array when an optimized image reconstruction is used. Significant improvements in parallel imaging performance were also obtained, including reduced g-factors for x and y accelerations.

Acknowledgments

References

1. Wright SM, Wald LL. Theory and application of array coils in MR spectroscopy. NMR Biomed 1997;10:394–410. [PubMed: 9542737]

2. Wiggins GC, Triantafyllou C, Potthast A, Reykowski A, Nittka M, Wald LL. 32-channel 3 Tesla receive-only phased-array head coil with soccer-ball element geometry. Magn Reson Med 2006;56:216–223. [PubMed: 16767762]

3. Moeller, S.; Van de Moortele, PF.; Adriany, G.; Snyder, C.; Andersen, PM.; Strupp, JP.; Vaughan, JT.; Ugurbil, K. Parallel imaging performance for densely spaced coils in phase arrays at ultra high field strength. Proceedings of the 12th Annual Meeting of ISMRM; Kyoto, Japan. 2004. (Abstract 2388)

4. Cline, H.; Sodickson, D.; Niendorf, T.; Giaquinto, R. 32-channel head coil array for highly accelerated parallel imaging applications. Proceedings of the 12th Annual Meeting of ISMRM; Kyoto, Japan. 2004. (Abstract 2387)

5. Wiggins, GC.; Wiggins, CJ.; Potthast, A.; Alagappan, V.; Kraff, O.; Reykowski, A.; Wald, LL. A 32 channel receive-only head coil and detunable transmit birdcage coil for 7 Tesla brain imaging. Proceedings of the 14th Annual Meeting of ISMRM; Seattle, WA, USA. 2006. (Abstract 415)

6. Adriany, G.; Gozubuyuk, A.; Auerbach, E.; Van de Moortele, PF.; Andersen, PM.; Vaughan, JT.; Ugurbil, K. A 32 channel transmit/receive transmission line head array for 3D RF shimming. Proceedings of the 15th Annual Meeting of ISMRM; Berlin, Germany. 2007. (Abstract 166)

7. Ledden, PJ.; Mareyam, A.; Wang, S.; Van Gelderen, P.; Duyn, JH. 32 Channel receive-only SENSE array for brain imaging at 7T. Proceedings of the 15th Annual Meeting of ISMRM; Berlin, Germany. 2007. (Abstract 242)

8. Zhu Y, Hardy CJ, Sodickson DK, Giaquinto RO, Dumoulin CL, Kenwood G, Niendorf T, Lejay H, McKenzie CA, Ohliger MA, Rofsky NM. Highly parallel volumetric imaging with a 32-element RF coil array. Magn Reson Med 2004;52:869–877. [PubMed: 15389961]

9. Hardy CJ, Darrow RD, Saranathan M, Giaquinto RO, Zhu Y, Dumoulin CL, Bottomley PA. Large field-of-view real-time MRI with a 32-channel system. Magn Reson Med 2004;52:878–884. [PubMed: 15389946]

10. Niendorf T, Hardy CJ, Giaquinto RO, Gross P, Cline HE, Zhu Y, Kenwood G, Cohen S, Grant AK, Joshi S, Rofsky NM, Sodickson DK. Toward single breath-hold whole-heart coverage

coronary MRA using highly accelerated parallel imaging with a 32-channel MR system. Magn Reson Med 2006;56:167–176. [PubMed: 16755538]

11. Reeder SB, Wintersperger BJ, Dietrich O, Lanz T, Greiser A, Reiser MF, Glazer GM, Schoenberg SO. Practical approaches to the evaluation of signal-to-noise ratio performance with parallel imaging: application with cardiac imaging and a 32-channel cardiac coil. Magn Reson Med 2005;54:748–754. [PubMed: 16088885]

12. Lanz, T.; Kellman, P.; Nittka, M.; Greiser, A.; Griswold, MA. A 32 channel cardiac array optimized for parallel imaging. Proceedings of the 14th Annual Meeting of ISMRM; Seattle, WA, USA. 2006. (Abstract 2578)

13. McDougall MP, Wright SM. Phase compensation in single echo acquisition imaging. Phase effects of voxel-sized coils in planar and cylindrical arrays. IEEE Eng Med Biol Mag 2005;24:17–22. [PubMed: 16382800]

14. McDougall MP, Wright SM. 64-channel array coil for single echo acquisition magnetic resonance imaging. Magn Reson Med 2005;54:386–392. [PubMed: 16032696]

15. Wiggins, G.; Potthast, A.; Triantafyllou, C.; Lin, FH.; Benner, T.; Wiggins, CJ.; Wald, LL. A 96-channel MRI system with 23- and 90-channel phase array head coils at 1.5 Tesla. Proceedings of the 13th Annual Meeting of ISMRM; Miami Beach, FL, USA. 2005. (Abstract 671)

16. Wiggins, GC.; Alagappan, V.; Potthast, A.; Schmitt, M.; Wiggins, CJ.; Fischer, H.; Jahns, K.; Benner, T.; Polimeni, J.; Wald, LL. Design optimization and SNR performance of 3T 96 channel phased array head coils. Proceedings of the 15th Annual Meeting of ISMRM; Berlin, Germany. 2007. (Abstract 243)

17. Schmitt M, Potthast A, Sosnovik DE, Polimeni J, Wiggins GC, Triantafyllou C, Wald LL. A 128-channel receive-only cardiac coil for highly accelerated cardiac MRI at 3 Tesla. Magn Reson Med 2008;59:1431–1439. [PubMed: 18506789]

18. Hardy, CJ.; Giaquinto, RO.; Piel, JE.; Rohling, KW.; Marinelli, L.; Fiveland, EW.; Rossi, CJ.; Park, KJ.; Darrow, RD.; Watkins, RD.; Foo, TK. 128-channel body MRI with a flexible high-density receiver-coil array. Proceedings of the 15th Annual Meeting of ISMRM; Berlin, Germany. 2007. (Abstract 244)

19. Wiesinger, F. Parallel magnetic resonance imaging: potential and limitations at high field [Dissertation]. Zurich: Swiss Federal Institute of Technology; 2005.

20. Wiesinger, F.; DeZanche, N.; Pruessmann, KP. Approaching ultimate SNR with finite coil arrays. Proceedings of the 13th Annual Meeting of ISMRM; Miami Beach, FL, USA. 2005. (Abstract 672)

21. Potthast, A.; Kalnischkies, B.; Kwapil, G.; Wald, LL.; Heumann, T.; Helmecke, S.; Schor, S.; Pirkl, G.; Buettner, M.; Schmitt, M.; Mattauch, G.; Hamm, M.; Stransky, P.; Baumgartl, R.; Hebrank, F.; Peyerl, M. A MRI system with 128 seamlessly integrated receive channels. Proceedings of the 15th Annual Meeting of ISMRM; Berlin, Germany. 2007. (Abstract 246)

22. British Standards Organization. Head forms for use in testing of protective helmets. London: British Standards Organization; 1995.

23. Hergt, M.; Oppelt, R.; Vester, M.; Reykowski, A.; Huber, KM.; Jahns, K.; Fischer, H. Low noise preamplifier with integrated cable trap. Proceedings of the 15th Annual Meeting of ISMRM; Berlin, Germany. 2007. (Abstract 1037)

24. Matschl, V.; Jahns, K.; Reykowski, A. Novel spine and body coil designs using matrix clusters and mode combiners. Proceedings of the 12th Annual Meeting of ISMRM; Kyoto, Japan. 2004. (Abstract 1586)

25. Kellman P, McVeigh ER. Image reconstruction in SNR units: a general method for SNR measurement. Magn Reson Med 2005;54:1439–1447. [PubMed: 16261576]

26. Roemer PB, Edelstein WA, Hayes CE, Souza SP, Mueller OM. The NMR phased array. Magn Reson Med 1990;16:192–225. [PubMed: 2266841]

27. Constantinides CD, Atalar E, McVeigh ER. Signal-to-noise measurements in magnitude images from NMR phased arrays. Magn Reson Med 1997;38:852–857. [PubMed: 9358462]

28. Wiesinger F, Boesiger P, Pruessmann KP. Electrodynamics and ultimate SNR in parallel MR imaging. Magn Reson Med 2004;52:376–390. [PubMed: 15282821]

29. Pruessmann KP, Weiger M, Scheidegger MB, Boesiger P. SENSE: sensitivity encoding for fast MRI. Magn Reson Med 1999;42:952–962. [PubMed: 10542355]

30. King, KF.; Angelos, L. SENSE image quality improvement using matrix regularization. Proceedings of the 9th Annual Meeting of ISMRM; Glasgow, Scotland. 2001. (Abstract 1771)

31. Duensing GR, Brooker HR, Fitzsimmons JR. Maximizing signal-to-noise ratio in the presence of coil coupling. J Magn Reson B 1996;111:230–235. [PubMed: 8661287]

32. Possanzini, C.; Boutelje, M. Influence of magnetic field on preamplifiers using GaAs FET technology. Proceedings of the 16th Annual Meeting of ISMRM; Toronto, Ontario, Canada. 2008. (Abstract 1123)

33. King, S. Zero shared resistance between coil elements of a phased array?. Proceedings of the 8th Annual Meeting of ISMRM; Denver, CO, USA. 2000. (Abstract 1406)

34. Ohliger MA, Ledden P, McKenzie CA, Sodickson DK. Effects of inductive coupling on parallel MR image reconstructions. Magn Reson Med 2004;52:628–639. [PubMed: 15334584]

35. Reykowski A, Wright SM, Porter JR. Design of matching networks for low noise preamplifiers. Magn Reson Med 1995;33:848–852. [PubMed: 7651124]
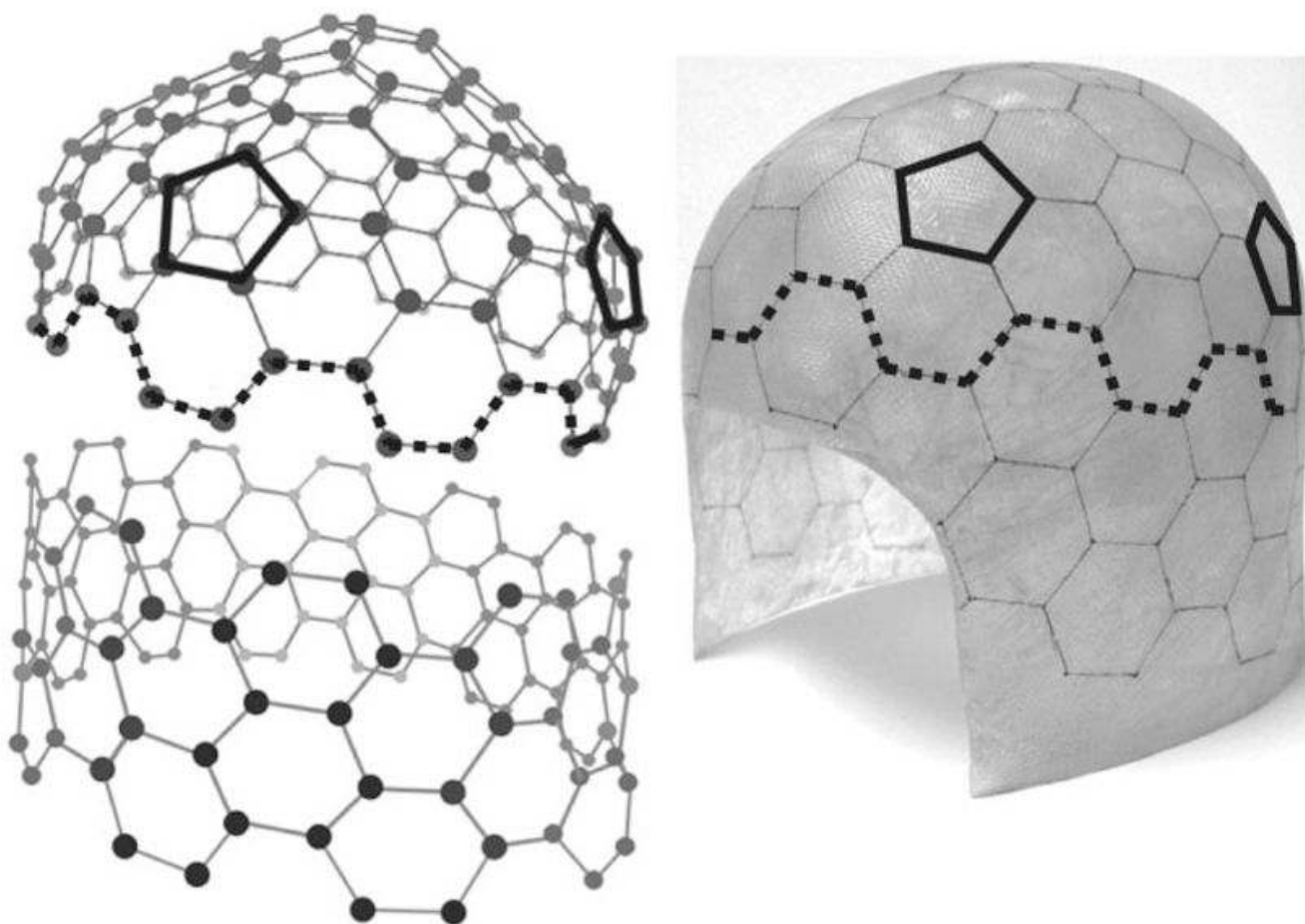
FIG. 1.
(top left) Schematic of molecular structure of one half of a C240 carbon "Buckyball" with two of the six pentagonal sections highlighted. (bottom left) Extension of hexagonal molecular structure onto a cylinder. (right) Fiberglass helmet with hexagonal and pentagonal tiling pattern drawn onto the helmet. Two centers of pentagonal symmetry are highlighted.
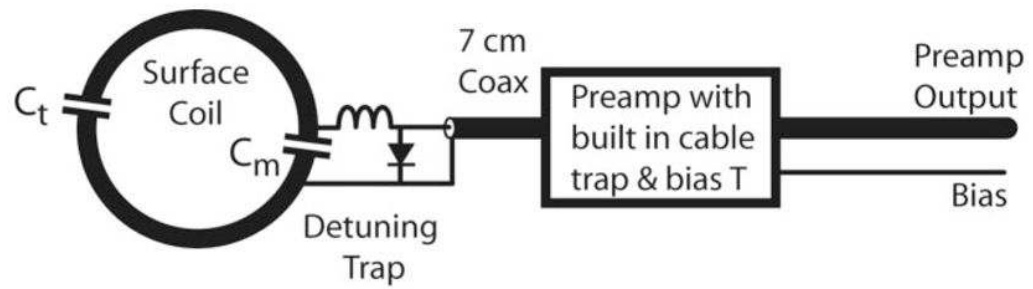
FIG. 2.
Circuit schematic for the surface coil and preamp chain. The coil element contains just two capacitors, C_t to control tuning and C_m to provide impedance transformation from the sample to the preamp. A diode detuning trap was formed around C_m. The preamp includes a cable trap for common mode rejection and a bias T.
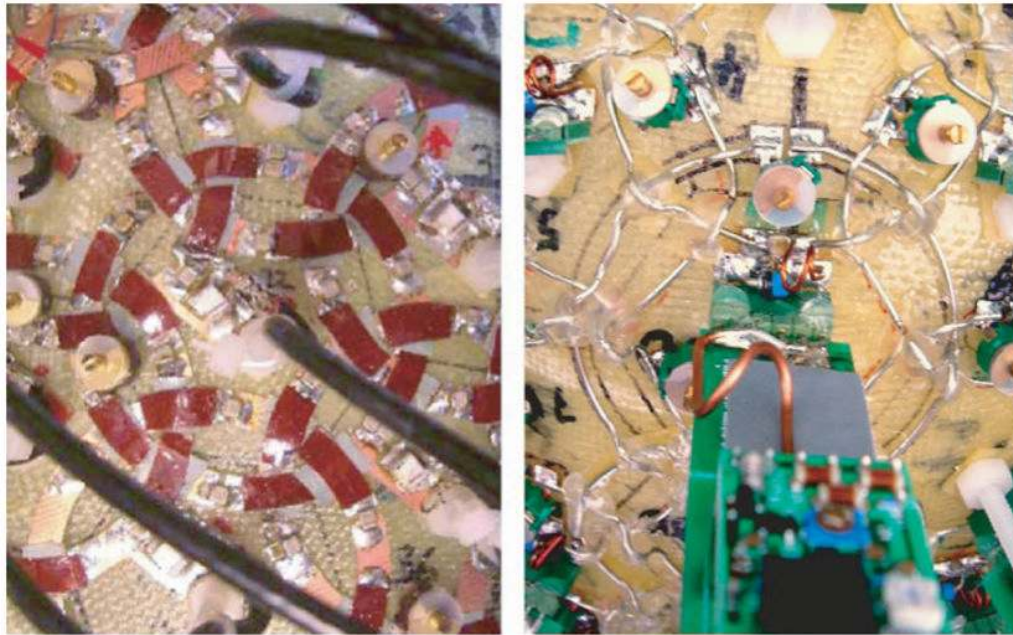
FIG. 3.
Close-ups of coil elements from two different designs. (left) FR4 circuit board elements with 5-mm track width. (right) Elements made from 18-awg wire. The circuit board design results in copper covering 59% of the surface area of the array, whereas the wire element design results in only 14% copper coverage, including pads.
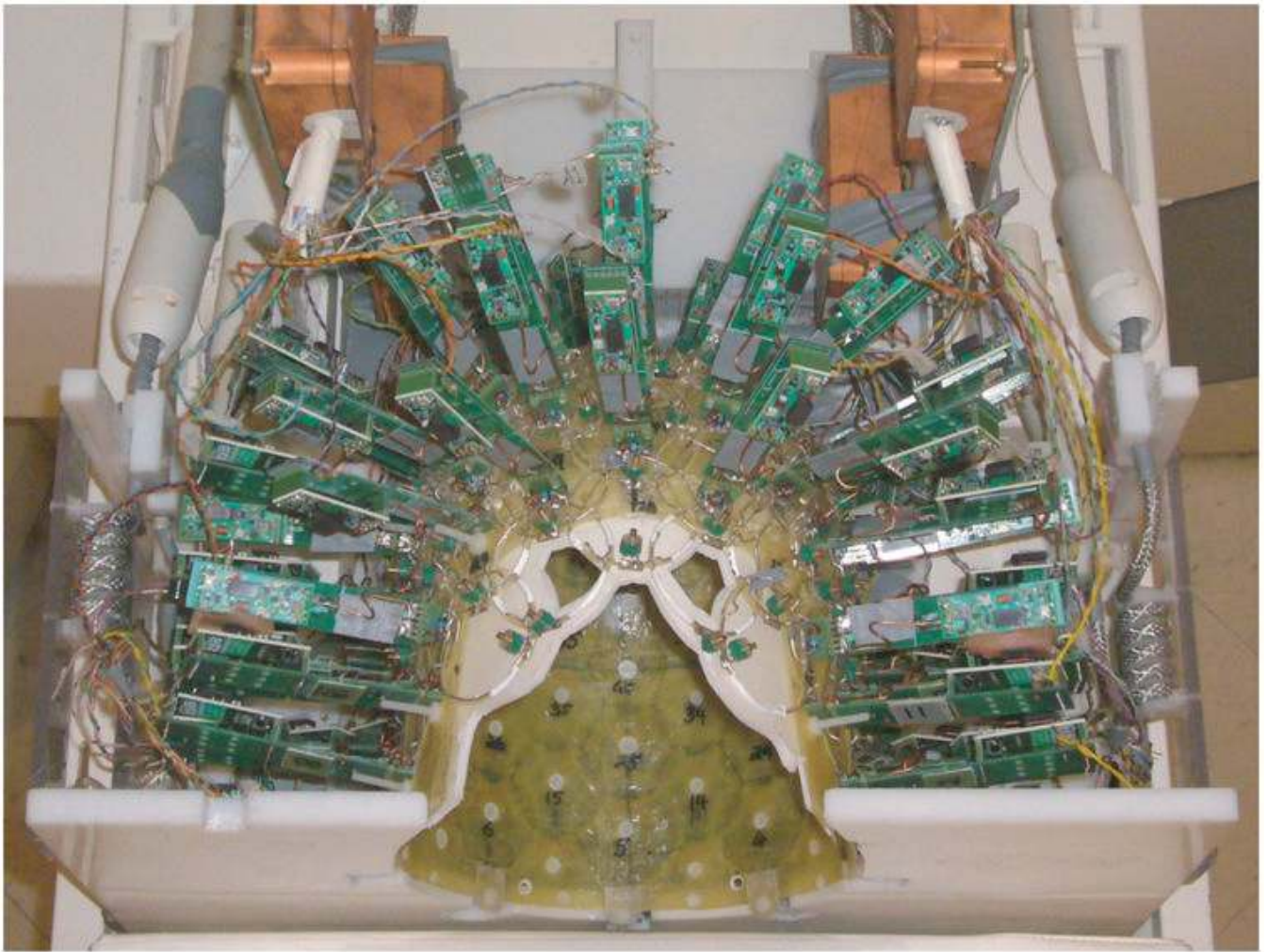
FIG. 4.
Completed coil array on scanner patient table. Preamp assemblies are mounted radially, and are each plugged into a socket at each coil element. The first 32 channels are received through plugs via sockets in the head end of the patient table. The additional 64 channels are received via coax bundles that run through the bore of the magnet. The copper boxes at the top of the image are common mode cable traps for these coax bundles.
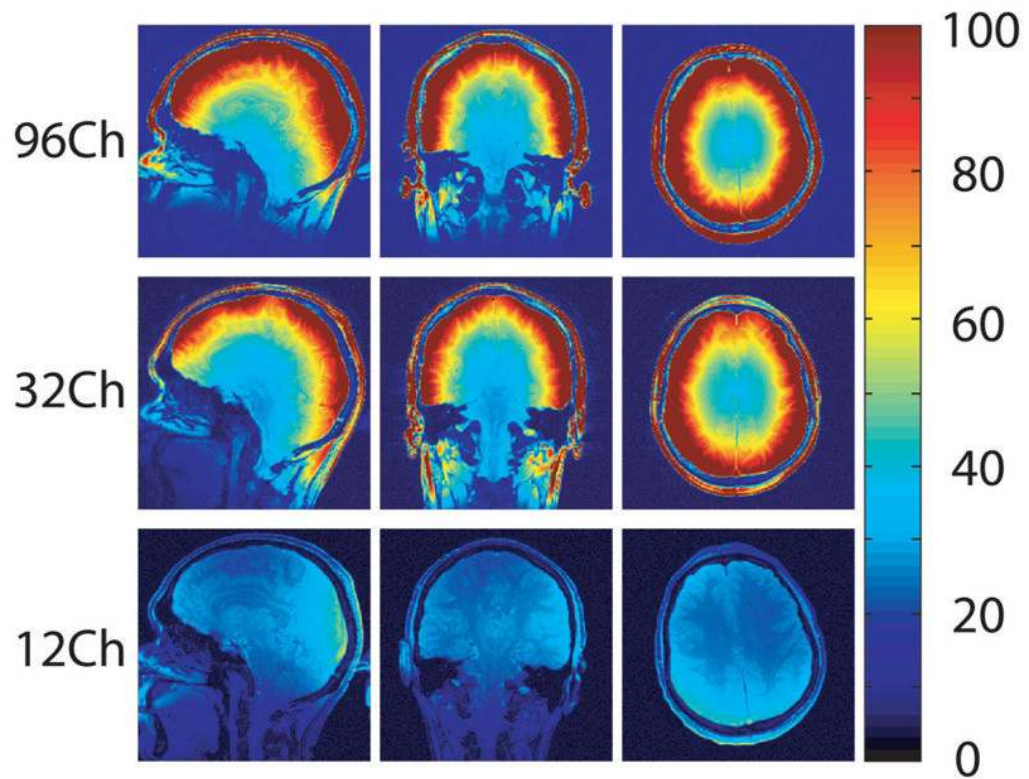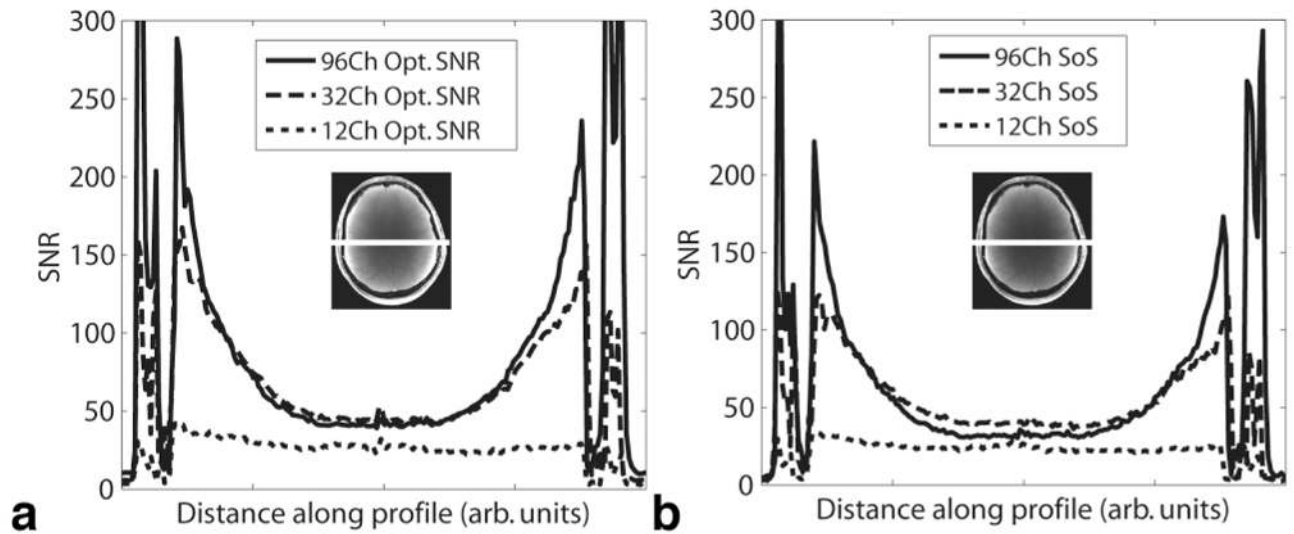
FIG. 5.
SNR maps for optimum SNR combination derived from gradient echo scans for (**a**) 96-channel coil; (**b**) 32-channel coil; and (**c**) commercial 12-channel coil. All maps are generated with the same color scale for comparison.

FIG. 6.
SNR profiles through axial slices passing approximately through the corpus callosum for the 96-channel coil (solid line), 32-channel coil (dashed line), and commercial 12-channel coil (dotted line). For optimum SNR combination (left) the central SNR is 5% lower for the 96-channel coil compared to the 32-channel coil, and 1.4-fold higher in the periphery of the brain. Both coils outperform the much larger 12-channel coil. For root-sum-of-squares combination (right) the central SNR for the 96-channel coil is 20% lower than the 32-channel coil, but it still outperforms the 32-channel coil in the periphery.
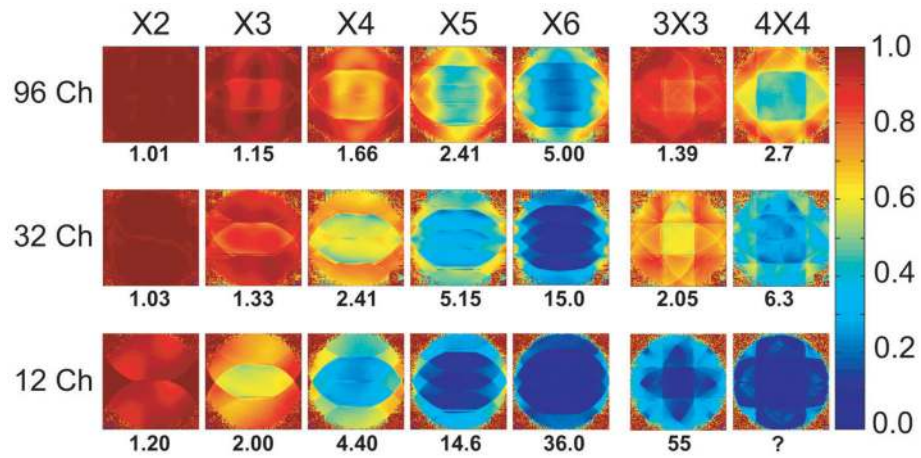
FIG. 7.
Maps of the inverse *g*-factor (1/*g*) at various one-dimensional and two-dimensional accelerations for the 96-channel coil (top row), the 32-channel coil (middle row), and the commercial 12-channel coil (bottom row), measured in a spherical "Braino" phantom. All maps are rendered with the same color scale for comparison; low values (blue) show areas with high *g*-factor. Peak *g*-factor values for each case are shown below each map.
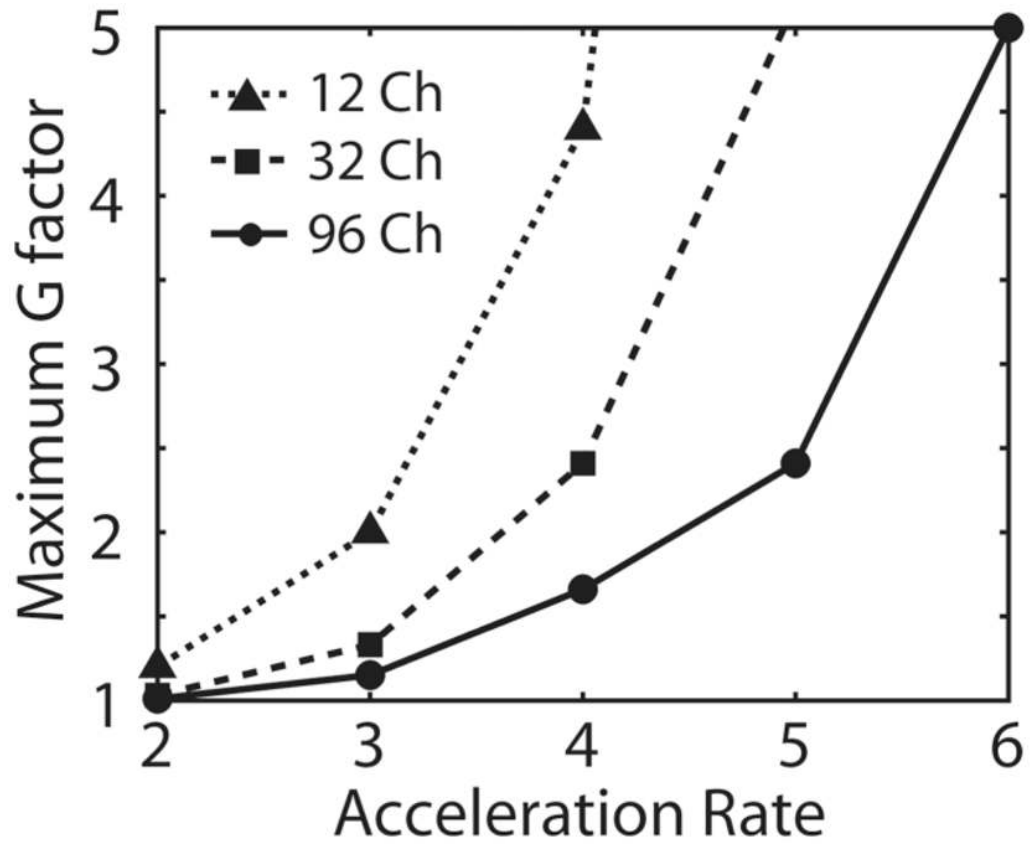
FIG. 8.
Maximum *g*-factor as a function of acceleration for the 12-channel (dotted line), 32-channel (dashed line), and 96-channel (solid line) coils. Substantial reductions in *g*-factor are obtained by increasing the number of coil elements.
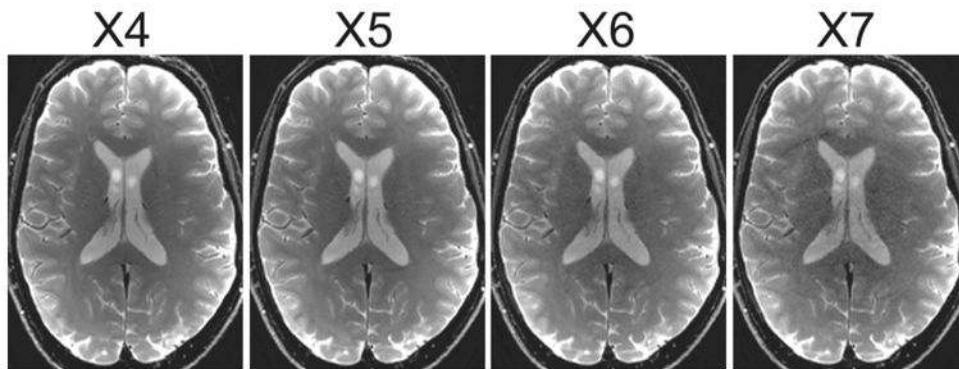
FIG. 9.
High-resolution single-shot encoded spin-echo EPI images with GRAPPA acceleration factors from 4 to 7 in the anterior–posterior direction obtained with the 96-channel coil (1 × 1 × 2 mm^3, matrix size = 224 × 224, TR/TE/flip angle = 4000 ms/63 ms/90°, BW = 1065 Hz/pixel, averages = 16).

Table 1

Dimensions of Coils Used in This Study (mm)

Coil	AP	LR	SI
96-channel helmet coil	222	181	200
32-channel helmet coil	222	181	220
Commercial 12-channel coil	270	250	270

AP = anterior–posterior, LR = left–right, SI = superior–inferior.

Table 2

Q_{UL}/Q_L for Various Coil Element Designs[*]

Coil	Material	Conductor width (mm)	Inner diameter (mm)	Number of capacitors	Q_{UL}	Q_L	Q_{UL}/Q_L
1	FR4	2.5	49	6	238	80	3.0
	With conductors from surrounding elements				216	75	2.9
2	FR4	5.0	47	6	265	71	3.7
	With conductors from surrounding elements				219	65	3.4
3	FR4	5.0	47	2	392	78	5.0
	With conductors from surrounding elements				277	71	3.9
4	18-awg wire	1.15	50	2	394	96	4.1
	With conductors from surrounding elements				374	94	4.0
5	11-awg wire	2.3	50	2	460	90	5.1

[*] Inner diameters were adjusted so that when two elements overlap to minimize inductive coupling, the spacing between coil centers remains equal to 38.9 mm.